IEEE Access
Multidisciplinary | Rapid Review | Open Access Journal

Received May 18, 2022, accepted June 2, 2022, date of publication June 6, 2022, date of current version June 13, 2022.

Digital Object Identifier 10.1109/ACCESS.2022.3180494

Numerical Analysis of RF-Induced Heating While Wearing Face Mask at Magnetic Resonance Imaging

YOUNGDAE CHO[1], (Graduate Student Member, IEEE), AND HYOUNGSUK YOO[1,2], (Senior Member, IEEE)
[1]Department of Electronic Engineering, Hanyang University, Seoul 04763, South Korea
[2]Department of Biomedical Engineering, Hanyang University, Seoul 04763, South Korea

Corresponding author: Hyoungsuk Yoo (hsyoo@hanyang.ac.kr)

This work was supported by the Institute for Information and Communications Technology Promotion (IITP) Grant funded by the Korea Government (Ministry of Science and ICT) (Development of Precision Analysis and Imaging Technology for Biological Radio Waves) under Grant 2021-0-00490.

ABSTRACT In response to the unprecedented COVID-19 pandemic, wearing face masks in public places and common facilities has been strongly recommended to help prevent the further spread of the virus. However, conductive components of the face mask carry the potential risk of radio-frequency (RF)-induced heating when exposed to an RF electromagnetic field, particularly during magnetic resonance imaging (MRI). In this study, a realistic human head model wearing a face mask exposed to a strong RF electromagnetic field in 1.5 T, 3 T, and 7 T MRI was simulated. A nose wire in contact with the skin and a mask sheet with relatively high electrical conductivity, emulating a silver nanoparticle-coated face mask, was modeled to investigate the worst case of RF-induced heating that could occur during the MRI scan. 24 scenarios were simulated by using finite-difference time-domain (FDTD)-based electromagnetic solver and thermal-transient solver from Sim4Life commercial simulation software. According to the results, a notable enhancement in the specific absorption rate (SAR) and temperature rise was observed in the local region of the skin where the wire contacted the skin around the edge of the high-conductive mask sheet. In particular, a maximum of a 12-fold increase in mass-averaged SAR and a temperature increase of more than 8.0°C occurred because of the conductive face mask at 3 T, compared to the normal polymer-based face mask with low conductivity. Our results confirmed that the degree of RF-induced heating due to the face mask could be completely different depending on the RF frequency of the MRI, location where the nose wire contacted the skin, and conductivity of the mask sheet. To the best of our knowledge, this is the first study to assess the face mask as a factor for RF-induced heating during MRI. These findings are important for providing a safety guide that allows patients to safely undergo MRI while wearing a face mask during the COVID-19 pandemic.

INDEX TERMS COVID-19, face mask, magnetic resonance imaging (MRI), radiofrequency (RF) heating, specific absorption rate (SAR).

I. INTRODUCTION

Magnetic resonance imaging (MRI) has become a key imaging modality in modern medicine as it can obtain high-resolution images of soft tissues without exposing the patient to ionizing radiation [1]. However, there is a safety issue called radio-frequency (RF)-induced heating owing to the time-varying electromagnetic (EM) field generated from MRI [2]. A magnetic field B_1 with a frequency of hundreds of MHz is created by an RF coil acting as an antenna of the MRI to obtain the MR image. Inevitably, a time-varying electric field is formed when a time-varying magnetic field is produced, causing biological tissues to absorb the energy from this EM field. The tissue temperature rises when the energy exceeds the thermo-regulation capability of the tissue, which leads to tissue damage [3]–[9]. Specifically, if a

The associate editor coordinating the review of this manuscript and approving it for publication was Santosh Kumar.

metallic component is in contact with or inserted into the human body, the electric current induced on the component surface is transferred to the contacted tissue, significantly increasing the risk of heating [10]–[22]. Therefore, metallic accessories, such as necklaces or earrings, are removed before MRI, and patients with implanted medical devices can only undergo MRI under controlled imaging protocols.

Recently, in response to the unprecedented COVID-19 pandemic, wearing face masks in medical facilities has been strongly recommended to help prevent the spread of the virus. However, the conductive nose wire for fixing the mask to the face and the mask sheet coated with silver nanoparticles for antibacterial and antiviral purposes [23] may increase the risk of RF-induced heating owing to their high electrical conductivity. Although the risk of heating caused by the metallic components of face masks during MRI was considered based on some reports [24]–[26], and the effect of wearing face mask on the MR image was analyzed [27], [28], no numerical studies have been conducted to estimate the RF-induced heating due to the face mask. In this study, a realistic human head model wearing a face mask inside an RF coil for 1.5 T, 3 T, and 7 T MRI was modeled and simulated to estimate RF-induced heating caused by wearing a face mask during the MRI. The specific absorption rate (SAR) and temperature increase according to the location of the nose wire and electrical conductivity of the mask sheet (a total of 24 scenarios) were calculated to investigate the RF-induced heating mechanism caused by the face mask and determine the worst case scenario that could occur in the clinic.

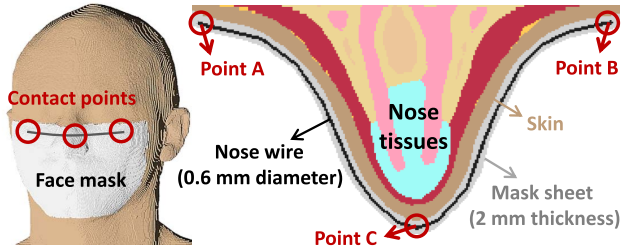

Contact type	No contact	Center	Single end	Both ends
Contact location	None	Point C	Point B	Points A & B

FIGURE 1. Simulation modeling of a realistic human head wearing a face mask and three types of nose wires in contact with the skin to find out the worst case of RF-induced heating caused the nose wire.

II. METHODOLOGY

A. HUMAN HEAD MODEL WEARING A FACE MASK

A human head wearing a face mask was modeled, as shown in Fig. 1. A heterogeneous realistic human model composed of 80 different types of tissues (DUKE model: male, 32 years old [29]) was used as the head model. According to the IT'IS database [30] as shown in Table 1, the permittivity and electrical conductivity of the tissues were assigned to the desired frequency. The face mask was modeled as a thin rectangular polypropylene (PP) sheet ($\varepsilon_r = 2.2$, σ=1e-14 S/m), the main raw material of the mask filter and woven fabric, with a thickness of 2 mm wrapped around most of the face from the middle of the nose to the chin. A perfect electric conductor (PEC) wire, with a length of 105 mm and diameter of 0.6 mm, was inserted into the mask sheet as the nose wire of the mask and was fully covered with a mask sheet to prevent contact with the skin. However, three cases where the center, single-end, and both ends of the wire were in contact with the skin were also modeled, assuming a worst-case scenario regarding the nose wire. The location where the wire made contact, according to each contact type, is shown on the right side of Fig. 1.

When analyzing RF-induced heating due to a face mask, the conductive mask sheet should also be considered a risk factor. Some face mask products are coated with silver nanoparticles for antibacterial and antiviral purposes. Silver nanoparticles are microscopic in size, making it difficult to determine their presence with the naked eye. In addition, owing to the diamagnetic properties of silver nanoparticles, there is no pulling or pushing effect due to the strong magnetic field of MRI, increasing the probability that a patient wearing a conductive face mask receives an MRI scan without being pre-screened by an MRI technician. It is impossible to model silver particles at the nanometer scale and the detailed textile patterns of the face mask in the numerical simulation. In this study, the best alternative in a simulation was emulating the silver nanoparticle-coated face mask based on a mask sheet model with an conductivity of 10 S/m as references [31]–[33] for a worst-case scenario regarding the silver nanoparticle-coated mask sheet.

B. RF HEAD COIL

For the RF electromagnetic source for 1.5 T, 3 T, and 7 T MRI, an RF birdcage head coil and an eight-channel RF transmit head coil were modeled as shown in Fig. 2. The RF coil for 1.5 T and 3 T MRI was a high-pass birdcage RF head coil, as shown in Fig. 2(a), with a height and diameter of 260 mm and 355 mm, respectively [34], [35]. The coil comprised 16 legs, each with a width of 15 mm and length of 230 mm, with two end rings, each 15 mm wide. 32 capacitors of 50.6 pF and 11.3 pF were placed in the middle of each end-ring segment to match the resonance frequencies of 64 MHz and 128 MHz for 1.5 T and 3 T MRI, respectively. The metallic components of the RF coil are simplified as PECs. The coil was driven using two harmonic current sources placed on the same end-ring for quadrature excitation.

As the uniformity of the B_1 field at 7 T degrades due to its shorter wavelength, a multi-channel RF coil usually mitigates the inhomogeneity of the B_1 field by varying the amplitudes and phases of the currents driving each channel. In this study, a multi-channel RF head coil composed of eight microstrip transmission line (MTL) resonator, as shown in Fig. 2 (b), was modeled for 7 T MRI based on the prior research conducted [36]. An MTL path with a width of 18 mm and a finite ground plane was employed on a Teflon substrate

TABLE 1. Assigned electrical properties of major tissues inside the human head model for electromagnetic simulation.

Model	Mass density (kg/m^3)	Relative permittivity ε_r			Electrical conductivity σ (S/m)		
		64 MHz	128 MHz	298 MHz	64 MHz	128 MHz	298 MHz
Skull	1908	16.68	14.73	13.44	0.06	0.07	0.08
Muscle	1090	72.23	63.56	58.22	0.69	0.72	0.77
CSF	1007	97.31	84.19	72.78	2.07	2.14	2.22
Skin	1109	92.17	65.65	49.90	0.44	0.52	0.64
Grey matter	1045	97.43	73.71	60.09	0.51	0.59	0.69
White matter	1041	67.84	52.65	43.82	0.29	0.34	0.41
Fat	911	13.64	12.38	11.75	0.07	0.07	0.08

* CSF : Cerebrospinal fluid

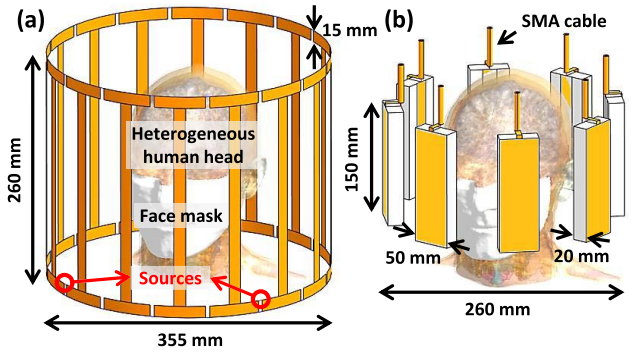

FIGURE 2. Simulation modeling of birdcage RF head coil for 1.5 T and 3 T MRI, and eight-channel RF transmit head coil for 7 T MRI. The total input power of the RF coils was scaled to ensure the whole head averaged SAR (*wh*SAR) was 3.2 W/kg.

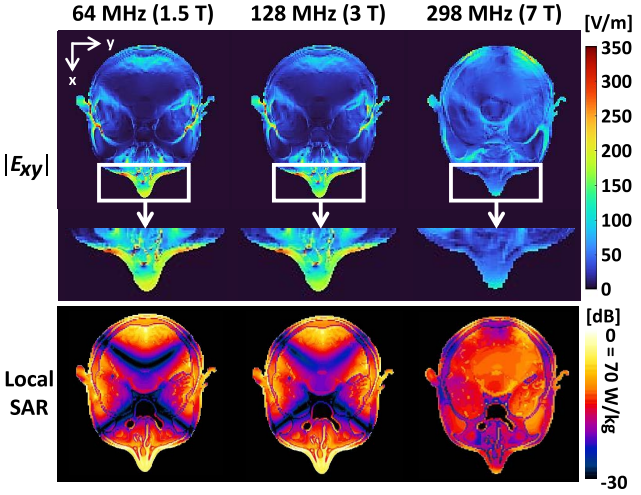

FIGURE 3. Horizontal slices of transverse electric field E_{xy} generated by the RF coil and local SAR on the human head without wearing a face mask.

(ε_r = 2.08, σ=0.000462 S/m) with width, length, and thickness of 150, 50, and 20 mm, respectively. Two capacitors were used at the ends of the resonator, and a single capacitor was used in series with the input source (SMA cable) to match the frequency of 298 MHz for the 7 T MRI. There was a successive phase delay of 45° between adjacent sources with the same magnitude for the circularly polarized excitation of the multi-channel RF coil. The total input powers of RF head coils for the scenarios of 1.5 T, 3 T, and 7 T MRI were scaled such that the whole head averaged SAR (*wh*SAR) was 3.2 W/kg for when the RF coil was operating at maximum allowable power, satisfying the safety guidelines for clinical settings.

C. SIMULATION SETUP

All numerical simulations of a masked human head with an RF head coil were performed using the finite-difference time-domain (FDTD)-based commercial software Sim4Life (Zurich Medtech, AG, Switzerland) [37]. The simulation times were set to 30 periods to achieve a convergence below -20 dB. The maximum grid steps were 2 mm × 2 mm × 2 mm for the head model. A fine grid with minimum steps of 0.25 mm × 0.25 mm × 0.25 mm was set for the region of the nose wire to analyze the effect of the nose wire more accurately. A high-performance GPU (GeForce RTX 3070 Ti 8 GB, NVIDIA, Medford, MA) and a deca-core CPU (3.0 GHz Intel Xeon W-2150B) were used to sample and calculate the models.

III. RESULTS AND DISCUSSION

A. RF ELECTRIC FIELDS GENERATED BY THE RF COIL AT DIFFERENT RESONANCE FREQUENCIES

Fig. 3 shows slices of the transverse electric field (E_{xy}) generated by the RF coil and local SAR according to the frequencies of the RF field when the human head model without a face mask was loaded. The slices were obtained from the horizontal and coronal planes passing through the geometrical center of the RF coil. According to the results, the strong E_{xy} and local SAR at 1.5 T and 3 T were distributed locally on the surface of the human head, such as skin and muscle where the face mask was in contact. However, at 7 T, the strong E_{xy} and local SAR were distributed deeper inside

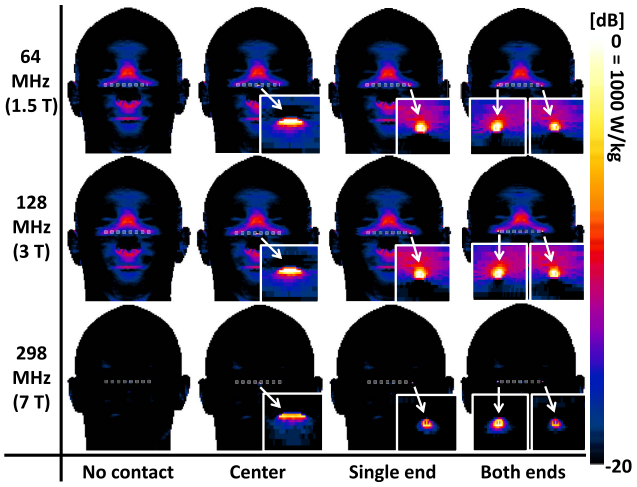

FIGURE 4. Local SAR on the surface of the human head according to the frequencies of RF field and different contact scenarios of a nose wire. 1000 W/kg was normalized to 0 dB. The location of nose wire for each case was indicated using a dashed line.

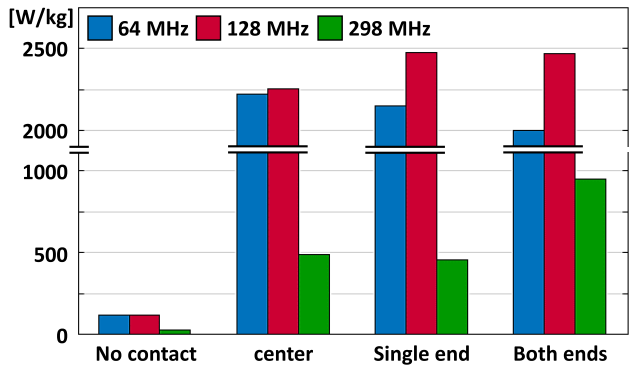

FIGURE 5. Peak of local SAR on the surface of the head for each scenario depicted in Fig. 4.

the human head, which has little relevance to the region in contact with the face mask, such as brain tissues. The primary reason for the difference in the E field distribution inside the human head is the difference in the wavelength of the B_1 signal for 1.5 T, 3 T, and 7 T MRI. It can be inferred from these results that RF heating mainly occurring at the skin by the face mask can be worse at 1.5 T and 3 T than at 7 T for the same total amount of energy absorbed by the human head.

B. SAR INCREASE DUE TO THE NOSE WIRE

Figs. 4 and 5 show the surface view of the local SAR maps of the human head and the bar graph of the maximum values for each case, respectively. An extremely high local SAR was observed in the local region where the nose wire made contact. In particular, as inferred from Fig. 3, the degree of local SAR increase was significantly greater at 1.5 T and 3 T when a stronger E_{xy} field was applied to the skin than at 7 T.

In the FDTD simulation, the size of a single voxel, a unit element in three-dimensional simulation, varied with the structural shape and complexity of the target

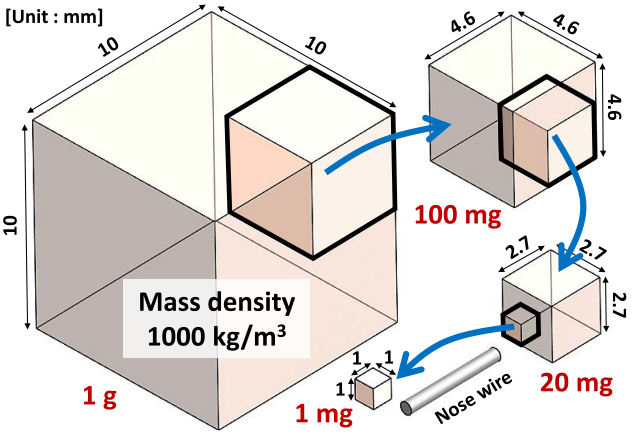

FIGURE 6. Size comparison between a nose wire and cubes with the mass density of 1000 kg/m3 according to the different masses.

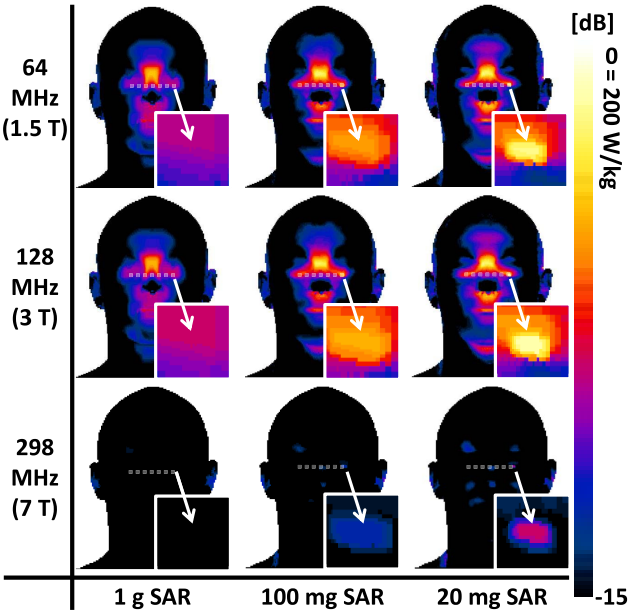

FIGURE 7. Mass-averaged SAR on the surface of the human head for the contact case of single end according to the different masses from 1 g to 20 mg. 200 W/kg was normalized to 0 dB. The location of nose wire for each case was indicated using a dashed line.

object, resulting in local SAR varying with the unit step of the voxel. Although this issue was prevented in this study by fixing the size of voxel around the nose wire to 0.25 mm × 0.25 mm × 0.25 mm, an excessively high local SAR as an outlier can occur due to a voxel protruding into a curved surface. Therefore, the averaged SAR from a cube of 1 g or 10 g, called 1 g SAR and 10 g SAR, respectively, is generally calculated for quantitative SAR comparison [38]–[40]. However, the increase in local SAR caused due to the nose wire was extremely localized at the point where the wire contacted it. Fig. 6 illustrates various cubes of a material as skin with a mass density of 1000 kg/m^3 to compare the size with that of a nose wire. Although the mass density of the skin in the simulation was

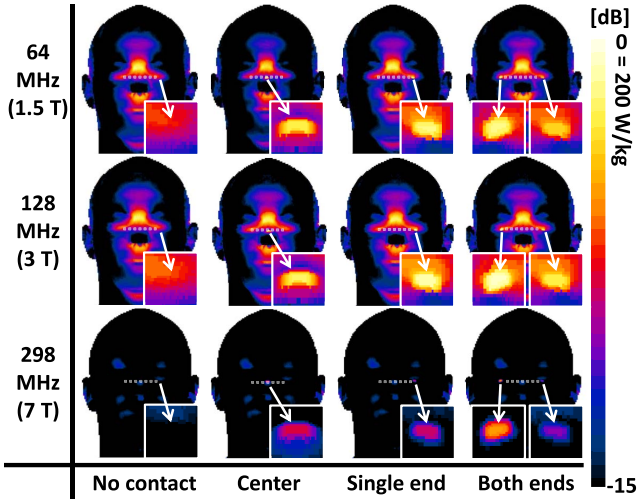

FIGURE 8. 20 mg SAR on the surface of the human head according to the frequencies of RF field and different contact scenarios of the nose wire. 200 W/kg was normalized to 0 dB. The location of nose wire for each case was indicated using a dashed line.

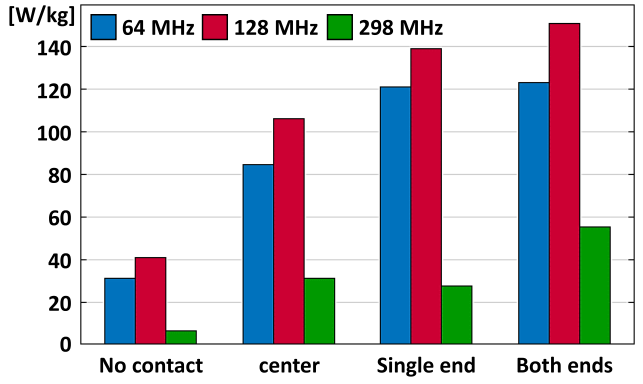

FIGURE 9. Peak of 20 mg SAR on the surface of the head for each scenario depicted in Fig. 8.

set to 1109 kg/m^3, it was set to 1000 kg/m^3 in Fig. 6 for convenience. According to the figure, the size of the 1 g cube was relatively large compared to that of the wire. Fig. 7 shows the surface view of the SAR maps of the human head with the case of single-end contact according to the average mass from 20 mg to 1 g. Regardless of the frequencies of the RF field, it is evident from the figure that 1 g SAR is not suitable for capturing the increase in SAR caused by the localized energy accumulation in the area where the nose wire touches the skin. Therefore, in this study, the averaged SAR from a cube of 20 mg mass (20 mg SAR) was calculated for comparing all scenarios because it accurately demonstrated the effect of the nose wire while offsetting the error in the local SAR. Note that 1 mg SAR was not obtained in this study because it requires sophisticated sampling with an extremely fine grid, exploiting the data size and calculation time.

Figs. 8 and 9 show 20 mg SAR maps for the contact cases of the wire depicted in Fig. 1 and a bar graph of the maximum values for each case, respectively. Regardless of the presence of the nose wire, a relatively higher SAR was observed around the ridge of the nose due to the intrinsic shape of the nose. According to the first column of Fig. 8, even if a conductive nose wire was included inside the mask, there was little effect on the SAR increase owing to the nose wire when it was fully insulated without contact. For the cases of contact at the center, single-end, and both ends, there was a drastic SAR increase in the local region where the wire was in contact. In particular, a high SAR above 100 W/kg was observed for the case with the contact at 1.5 T and 3 T than that at 7 T because a stronger E field was acting on the skin where the nose wire was located, resulting in more induced current at the nose wire. Moreover, the SAR increase by the nose wire in the same contact case may differ between 1.5 T, 3 T, and 7 T MRI because the antenna effect is maximized when the metallic wire has comparable lengths to the in-situ wavelengths of the RF signal generated by RF coil [22]. Regardless of the frequencies of the RF field, a large increase in SAR was observed in the case of contact at both ends than at the single-end and the center because the wire with both ends in contact with the skin forms a loop, thus increasing the amount of induced current flowing into the skin. In the case of contact at the center, the wire was electrically divided into two lines, owing to the contact with the skin, causing a decrease in the antenna effect and induced current at the wire. The results confirmed that the risk of RF-induced heating due to the face mask can be increased if the induced current flows into the skin by contact of the nose wire with the skin. A nose wire made of a material with low conductivity, such as silicon, or a nose wire with insulation coating, should be used to reduce this risk and prevent the induced current from flowing into the skin.

C. IMPACT OF THE CONDUCTIVE MASK SHEET

Although the conductivity of the silver nanoparticle-coated mask sheet is not as high as that of pure silver, a sheet with a conductivity of 10 S/m can be considered a conductor. To analyze the influence of the inside and outside of the mask sheet according to the conductivity of the mask sheet, E_{xy} map inside the mask sheet and the surface view of the volume current density of the mask sheet according to the conductivity are compared, as shown in Figs. 10 and 11, respectively. According to Fig. 10, in the mask sheet made of PP with very low conductivity (1e-14 S/m), the incident E field by the RF coil and the secondary E field generated by the induced current in the nose wire were distributed, creating a strong E field inside the mask sheet. However, in the nanoparticle-coated mask sheet with 10 S/m conductivity, the electromagnetic field does not penetrate inside the conductor due to the intrinsic property. The incident E field by the RF coil and the secondary E field by the induced current were hardly observed inside the conductive mask sheet. As shown in Fig. 11, in the mask sheet with low conductivity, there is almost no current flowing on the mask surface, similar to a dielectric insulator. However, a fairly strong induced current due to the incident E field was observed on the surface of coated mask sheet. Thus, it can be inferred from these results

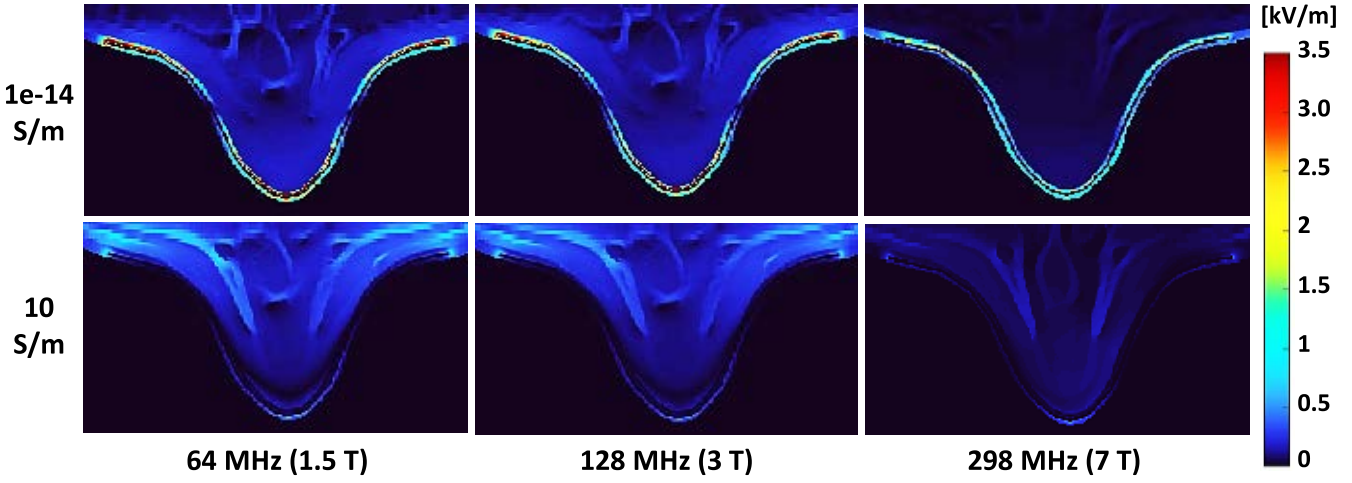

FIGURE 10. Horizontal slices of E_{xy} on the human head wearing a face mask according to the electric conductivity of the mask sheet and the frequencies of RF field. The location of the slice is the same as shown in Fig. 3. The nose wire of each case was fully covered by the mask sheet.

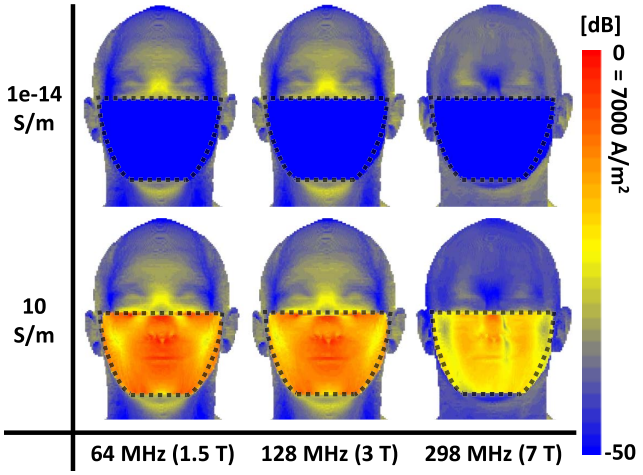

FIGURE 11. Volume current density on the surface of the mask sheet and human head according to the electric conductivity of the sheet and the frequencies of RF field. The location of mask sheet for each case was indicated by a dashed line.

that RF-induced heating by the silver nanoparticle-coated face mask is mainly caused by the current induced in the conductive mask sheet rather than the nose wire.

Fig. 12 shows the surface view of the 5 mg SAR of the human head according to mask sheet conductivity and RF field frequencies. All face masks for the scenarios in Fig. 12 include a nose wire without contact with the skin. Regardless of the frequencies of the RF field, the SAR of the skin underneath the mask sheet with a conductivity of 10 S/m was extremely low, except at the edge of the sheet, because of the shielding effect of the conductive sheet. However, on the skin (under the eyelids, chin, and sideburns) in contact with the edge of the mask, a drastic SAR increase was observed at 1.5 T and 3 T due to an induced current flowing on the surface of the conductive mask sheet, as depicted in Fig. 11. Compared to the cases at 1.5 T and 3 T, the SAR increase at 7 T due to the conductive mask sheet was inconspicuous because the relatively weak incident E field inducing the current on the surface of the conductive mask sheet was relatively low, as shown in Figs. 3 and 11. Fig. 13 shows the surface view of the 5 mg SAR according to the conductivity of the mask sheet and the contact cases of the nose wire at 3 T (128 MHz). As shown in Fig. 13, the SAR increase in the local region where the nose wire is in contact with the skin is obscured because the SAR increase due to the induced current on the conductive mask sheet is dominant. Fig. 14 shows a bar graph of the maximum 20 mg SAR for all 24 scenarios analyzed in this study. It is evident from the results that the risk of RF heating due to the conductive mask sheet with the silver nanoparticle coating could be much more severe than that caused by the conductive nose wire touching the skin. As mentioned in Section II-A, fibers and detailed textile patterns constituting the silver nanoparticle-coated face mask were simplified to a single sheet with high conductivity in this study due to the limitation of EM simulation. However, the reliability of the simulated results can be further improved by future work using advanced simulation techniques which can model and analyze fiber at nanometer scale and textile patterns of the mask sheet [41]–[44].

D. TEMPERATURE RISE DUE TO FACE MASK

According to the US Food and Drug Administration's (FDA) guidelines, temperature studies are recommended for RF safety assessment [45]. To calculate the temperature rise due to the face mask, the results of the EM simulations were coupled with a thermal-transient solver, employing the Pennes bioheat equation [46], [47], expressed as

$$\rho c \frac{\partial T}{\partial t} = \nabla \cdot (k \nabla T) + \rho Q + \rho S - H(T - T_b) \qquad (1)$$

where T is the temperature, t is the time, ρ is the volume density of the mass, c is the specific heat capacity, k is the thermal conductivity, Q is the metabolic heat generation rate, S is the SAR, and H is the heat transfer rate. The thermal properties

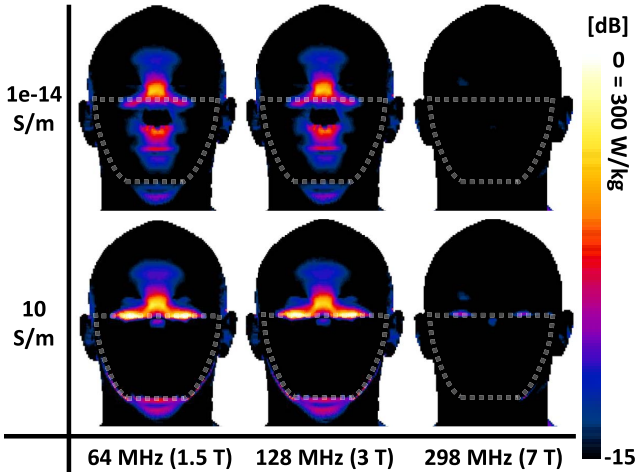

FIGURE 12. 20 mg SAR on the surface of the human head according to the frequencies of RF field and electric conductivity of the mask sheet. 300 W/kg was normalized to 0 dB. The location of mask sheet for each case was indicated using a dashed line.

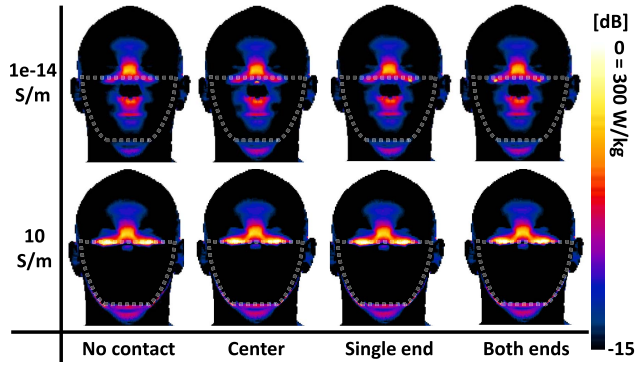

FIGURE 13. 20 mg SAR on the surface of the human head according to the electric conductivity of the mask sheet and different contact scenarios of the nose wire. 300 W/kg was normalized to 0 dB. The location of mask sheet for each case was indicated using a dashed line.

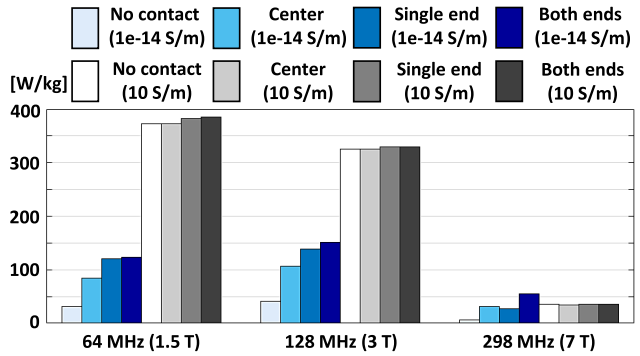

FIGURE 14. Peak of 20 mg SAR on the surface of the head for all 24 scenarios analyzed in this study.

of the head tissues from IT'IS database [30], as shown in Table 2, were applied to the thermal simulation. The results of the EM simulations were coupled with a thermal transient solver to calculate the temperature increase due to the face mask. The region of the thermal simulation was sampled using the same grid as that used in the EM simulations with the Neumann boundary condition; the heat flux moving through the boundary was zero. The initial temperature of

TABLE 2. Assigned thermal properties for major tissues inside the human head model for thermal-transient simulation.

Model	Specific heat capacity (J/kg/K)	Thermal conductivity (W/m/K)	Heat generation rate (W/kg)	Heat transfer rate ($W/m^3/K$)
Skull	1312	0.320	0.155	1288
Muscle	3421	0.495	0.906	2706
CSF	4096	0.573	0	0
Skin	3391	0.372	1.645	7969
Grey matter	3696	0.547	15.539	53880
White matter	3583	0.481	4.321	14931
Fat	2348	0.211	0.507	2013

TABLE 3. Degree of temperature rise for all scenarios analyzed in this study based on control group. The control group is a group of cases with a mask sheet with conductivity of 1e-14 S/m and a nose wire without skin contact.

σ (S/m)	Nose wire contact type	Maximum temperature rise (°C) compared to control group		
		64 MHz (1.5 T)	128 MHz (3 T)	298 MHz (7 T)
1e-14	No contact	Control group		
	Center	+1.0	+1.1	+0.5
	Single end	+1.1	+1.3	+0.3
	Both ends	+1.0	+1.2	+0.6
10	No contact	+8.2	+6.7	+0.7
	Center	+8.2	+6.7	+0.7
	Single end	+8.3	+6.8	+0.7
	Both ends	+8.3	+6.8	+0.7

the tissues was set to 37°C, and the boundary condition was set to ignore the heat diffusion by the temperature difference between the human body and the air, which occurs mainly on the surface of the skin.

Table 3 shows the degree of temperature rise for all cases based on the values for the cases in the first row of the table (conductivity of mask sheet=1e-14 S/m, nose wire without skin contact) as a control group. These cases were selected as the control group because the SAR for the control group was similar to the results when the face mask was not worn. Values in each row of the table were compared only with those in the same column (based on the same frequency of the RF field). The exposure time was set as 900 s. According to Table 3, the temperature rise in all cases at 7 T was lower than at 1.5 T and 3 T, and the degree was less than 1°C compared to the control group. In the case of mask sheet with 1e-14 S/m conductivity, the temperature rise due to the nose wire in contact with the skin was more than 1°C at 1.5 T and 3 T compared to the control group. However, the difference according to the contact type of the nose wire is insignificant. Note that

there is inevitable uncertainty of the numerical simulation that the value of temperature increase at a very local spot, such as the point where the nose wire made contact with the skin, may vary depending on the size of the unit step to sample the model. Therefore, we strongly recommend that patients undergoing MRI should wear a face mask without metallic nose wire even if calculated temperature increase by the nose wire in this study seems to be compliance with the localized temperature rise limit of 2 °C [48]. Regardless of the frequency of the RF field, the temperature increase due to the conductive mask sheet with 10 S/m was more severe than that of the normal mask sheet with 1e-14 S/m. In particular, at 1.5 T and 3 T, significant temperature increase of 8.2°C and 6.7°C, respectively, were observed compared to the control group. Contact of the nose wire with the skin had little effect on RF-induced heating by the silver nanoparticle-coated face mask because the RF energy deposition estimated by SAR was much more dominant for the conductive mask sheet than for the nose wire. The degree of temperature increase in the actual situation would be relatively lower than the calculated results because of thermal regulation through sweat and blood. Nevertheless, it is evident from the results that wearing silver nanoparticle-coated face mask in MRI causes temperature increase exceeding the safety limit.

IV. CONCLUSION

In this study, EM and thermal simulations were performed to quantitatively estimate the SAR and temperature increase caused by wearing a face mask during MRI at 1.5, 3, and 7 T. The nose wire in contact with the skin and mask sheet with relatively high electrical conductivity, emulating the silver nanoparticle-coated face mask, was modeled to investigate the worst-case of heating that could occur due to the face mask. A local increase in the SAR and temperature was observed in the contact area when the nose wire was partially in contact with the skin. Considering the uncertainty of the numerical simulation at a very local spot, wearing a face mask without metallic nose wire is strongly recommended in MRI even if calculated temperature increase caused by the nose wire in this study was compliance with the safety limit of 2°C. When the conductivity of the mask sheet was increased to 10 S/m, assuming that the face mask was coated with silver nanoparticles for antibacterial and antiviral purposes, a much higher SAR was observed at the edge of the mask. The temperature rise was over 8.2°C and 6.7°C for 1.5 T and 3 T, respectively, exceeding the safety limit. We can conclude from the results that wearing a face mask coated with silver nanoparticles in MRI has the worst effect on RF-induced heating compared to any other case that could be caused due to the face mask. For the conclusion of general safety of the face mask in MRI, follow-up studies to analyze the gradient-induced heating and effects depending on the head size, RF coil type, and excitation scheme are necessary. Although clinical trial in MRI could not be performed due to safety issues, numerical simulations using realistic human head model effectively analyzed the risk of RF-induced heating caused by face mask which could be occurred in real environments. MRI experiment using a head-mimicking gel phantom wearing a face mask can help to verify the simulated results and will be conducted as a future work. To the best of our knowledge, this is the first study to assess RF-induced heating caused by wearing a face mask during an MRI. We believe that these findings are useful in providing a safety guide that allows patients to safely undergo an MRI scan while wearing a face mask during the COVID-19 pandemic.

REFERENCES

[1] M. A. Brown, R. C. Semelka, and B. M. Dale, *MRI: Basic Principles and Applications*. Hoboken, NJ, USA: Wiley, 2015.

[2] L. P. Panych and B. Madore, "The physics of MRI safety," *J. Magn. Reson. Imag.*, vol. 47, no. 1, pp. 28–43, Jan. 2018.

[3] D. J. Schaefer, "Safety aspects of radiofrequency power deposition in magnetic resonance," *Magn. Reson. Imag. Clinics North Amer.*, vol. 6, no. 4, pp. 775–789, Nov. 1998.

[4] D. Formica and S. Silvestri, "Biological effects of exposure to magnetic resonance imaging: An overview," *Biomed. Eng. OnLine*, vol. 3, no. 1, pp. 3–11, Dec. 2004, doi: 10.1186/1475-925X-3-11.

[5] U. D. Nguyen, J. S. Brown, I. A. Chang, J. Krycia, and M. S. Mirotznik, "Numerical evaluation of heating of the human head due to magnetic resonance imaging," *IEEE Trans. Biomed. Eng.*, vol. 51, no. 8, pp. 1301–1309, Aug. 2004.

[6] M. Murbach, E. Zastrow, E. Neufeld, E. Cabot, W. Kainz, and N. Kuster, "Heating and safety concerns of the radio-frequency field in MRI," *Curr. Radiol. Rep.*, vol. 3, no. 12, p. 45, Dec. 2015, doi: 10.1007/s40134-015-0128-6.

[7] M. J. P. van Osch and A. G. Webb, "Safety of ultra-high field MRI: What are the specific risks?" *Current Radiol. Rep.*, vol. 2, no. 8, p. 61, Aug. 2014, doi: 10.1007/s40134-014-0061-0.

[8] F. G. Shellock, "Radiofrequency energy-induced heating during MR procedures: A review," *J. Magn. Reson. Imag.*, vol. 12, no. 1, pp. 30–36, 2000.

[9] R. AE Adair and R. C. Petersen, "Biological effects of radiofrequency/microwave radiation," *IEEE Trans. Microw. Theory Techn.*, vol. 50, no. 3, pp. 953–962, Mar. 2002.

[10] U.S. Department of Health and Human Services. (2014). *Guidance for Industry and FDA Staff: Establishing Safety and Compatibility of Passive Implants in the Magnetic Resonance (MR) Environment*. [Online]. Available: https://www.fda.gov

[11] R. Das and H. Yoo, "RF heating study of a new medical implant lead for 1.5 T, 3 T, and 7 T MRI systems," *IEEE Trans. Electromagn. Compat.*, vol. 59, no. 2, pp. 360–366, Apr. 2017.

[12] Y. Cho and H. Yoo, "RF heating of implants in MRI: Electromagnetic analysis and solutions," *Investigative Magn. Reson. Imag.*, vol. 24, no. 2, pp. 67–75, Jun. 2020.

[13] S. Hayat, Y. Cho, S. Oh, and H. Yoo, "RF-induced heating of various tattoos at magnetic resonance imaging systems," *IEEE Access*, vol. 9, pp. 100951–100961, 2021, doi: 10.1109/ACCESS.2021.3097145.

[14] L. Winter, F. Seifert, L. Zilberti, M. Murbach, and B. Ittermann, "MRI-related heating of implants and devices: A review," *J. Magn. Reson. Imag.*, vol. 53, no. 6, pp. 1646–1665, Jun. 2021.

[15] A. Gill and F. G. Shellock, "Assessment of MRI issues at 3-tesla for metallic surgical implants: Findings applied to 61 additional skin closure staples and vessel ligation clips," *J. Cardiovascular Magn. Reson.*, vol. 14, no. 1, p. 3, Dec. 2012, doi: 10.1186/1532-429X-14-3.

[16] S. M. Park, R. Kamondetdacha, A. Amjad, and J. A. Nyenhuis, "MRI safety: RF-induced heating near straight wires," *IEEE Trans. Magn.*, vol. 41, no. 10, pp. 4197–4199, Oct. 2005.

[17] X. Ji, J. Zheng, R. Yang, W. Kainz, and J. Chen, "Evaluations of the MRI RF-induced heating for helical stents under a 1.5 T MRI system," *IEEE Trans. Electromagn. Compat.*, vol. 61, no. 1, pp. 57–64, Feb. 2019.

[18] Q. Zeng, J. Liu, L. M. Angelone, T. Lloyd, S. Wedan, J. Chen, and W. Kainz, "Investigation of RF-induced heating near interventional catheters at 1.5 T MRI: A combined modeling and experimental study," *IEEE Trans. Electromagn. Compat.*, vol. 61, no. 5, pp. 1423–1431, Oct. 2019.

[19] J. Zheng, X. Ji, W. Kainz, and J. Chen, "Study on search strategies for assessing the worst case RF-induced heating for multi-configuration implant system under MRI," *IEEE Trans. Electromagn. Compat.*, vol. 62, no. 1, pp. 43–51, Feb. 2020.

[20] I. A. Shah and H. Yoo, "Assessing human exposure with medical implants to electromagnetic fields from a wireless power transmission system in an electric vehicle," *IEEE Trans. Electromagn. Compat.*, vol. 62, no. 2, pp. 338–345, Apr. 2020.

[21] I. A. Shah, Y. Cho, and H. Yoo, "Safety evaluation of medical implants in the human body for a wireless power transfer system in an electric vehicle," *IEEE Trans. Electromagn. Compat.*, vol. 63, no. 3, pp. 681–691, Jun. 2020.
[22] B. R. Steensma, J. P. Tokaya, P. R. S. Stijnman, M. A. Erturk, C. A. T. van den Berg, and A. J. E. Raaijmakers, "Effect of transmit frequency on RF heating on metallic implants," in *Proc. ISMRM Annu. Meeting*, May 2021.
[23] S. S. Jeremiah, K. Miyakawa, T. Morita, Y. Yamaoka, and A. Ryo, "Potent antiviral effect of silver nanoparticles on SARS-CoV-2," *Biochem. Biophys. Res. Commun.*, vol. 533, no. 1, pp. 195–200, Nov. 2020, doi: 10.1016/j.bbrc.2020.09.018.
[24] U.S. Department of Health and Human Services. (2020). *Wear Face Masks With no Metal During MRI Exams: FDA Safety Communication*. [Online]. Available: http://www.fda.gov
[25] M. C. Jaklevic, "Avoid masks with metal during magnetic resonance imaging," *JAMA*, vol. 325, no. 3, p. 214, Jan. 2021, doi: 10.1001/jama.2020.25687.
[26] J. D. Collins, H. Rowley, T. Leiner, S. Reeder, M. Hood, I. Dekkers, K. Tha, V. Gulani, and E. Kopanoglu, "Magnetic resonance imaging during a pandemic: Recommendations by the ISMRM safety committee," *J. Magn. Reson. Imag.*, vol. 55, no. 5, pp. 1322–1339, May 2022, doi: 10.1002/jmri.28006.
[27] C. S. W. Law, P. S. Lan, and G. H. Glover, "Effect of wearing a face mask on fMRI BOLD contrast," in *Proc. ISMRM Annu. Meeting*, May 2021, p. 1738.
[28] C. S. W. Law, P. S. Lan, and G. H. Glover, "Effect of wearing a face mask on fMRI BOLD contrast," *NeuroImage*, vol. 229, Apr. 2021, Art. no. 117752, doi: 10.1016/j.neuroimage.2021.117752.
[29] A. Christ, W. Kainz, E. G. Hahn, K. Honegger, M. Zefferer, E. Neufeld, W. Rascher, R. Janka, W. Bautz, J. Chen, B. Kiefer, P. Schmitt, H.-P. Hollenbach, J. Shen, M. Oberle, D. Szczerba, A. Kam, J. W. Guag, and N. Kuster, "The virtual family—Development of surface-based anatomical models of two adults and two children for dosimetric simulations," *Phys. Med. Biol.*, vol. 55, no. 2, pp. N23–N38, Jan. 2010.
[30] P. A. Hasgall, F. Di Gennaro, C. Baumgartner, E. Neufeld, B. Lloyd, M. C. Gosselin, D. Payne, A. Klingenböck, and N. Kuster. (Sep. 1, 2015). *ITIS Database for Thermal and Electromagnetic Parameters of Biological Tissues, Version 3.0*. [Online]. Available: http://www.itis.ethz.ch/database
[31] D. Shao, H. Zhang, L. Tao, K. Cao, and Q. Wei, "A facile approach for preparing ag functionalized nonwoven polypropylene membrane to improve its electrical conductivity and electromagnetic shielding performance," *Materials*, vol. 12, no. 2, p. 296, Jan. 2019, doi: 10.3390/ma12020296.
[32] J. Li, W.-J. Peng, Z.-J. Fu, X.-H. Tang, H. Wu, S. Guo, and M. Wang, "Achieving high electrical conductivity and excellent electromagnetic interference shielding in poly(lactic acid)/silver nanocomposites by constructing large-area silver nanoplates in polymer matrix," *Compos. B, Eng.*, vol. 171, pp. 204–213, Aug. 2019.
[33] L. Hu and Z. Kang, "Enhanced flexible polypropylene fabric with silver/magnetic carbon nanotubes coatings for electromagnetic interference shielding," *Appl. Surf. Sci.*, vol. 568, Dec. 2021, Art. no. 150845, doi: 10.1016/j.apsusc.2021.150845.
[34] L. Golestanirad, B. Keil, L. M. Angelone, G. Bonmassar, A. Mareyam, and L. L. Wald, "Feasibility of using linearly polarized rotating birdcage transmitters and close-fitting receive arrays in MRI to reduce SAR in the vicinity of deep brain simulation implants," *Magn. Reson. Med.*, vol. 77, no. 4, pp. 1701–1712, Apr. 2017.
[35] L. Golestanirad, L. M. Angelone, M. I. Iacono, H. Katnani, L. L. Wald, and G. Bonmassar, "Local SAR near deep brain stimulation (DBS) electrodes at 64 and 127 MHz: A simulation study of the effect of extracranial loops," *Magn. Reson. Med.*, vol. 78, no. 4, pp. 1558–1565, Oct. 2017.
[36] Y. Cho, A. Basir, and H. Yoo, "Adjustable RF transmitter head coil: Improving transmit efficiency with SAR management for 7-T magnetic resonance imaging," *IEEE Trans. Microw. Theory Techn.*, vol. 69, no. 5, pp. 2686–2696, May 2021, doi: 10.1109/TMTT.2021.3057620.
[37] *Sim4Life by ZMT*. [Online]. Available: http://www.zurichmedtech.com
[38] *Draft Standard for Determining the Peak Spatial Average Specific Absorption Rate (SAR) in the Human Body From Wireless Communications Devices, 30 MHz-6 GHz. Part 1: General Requirements for Using the Finite Difference Time Domain (FDTD) Method for SAR Calculations*, Standard IEC/IEEE P62704-1, International Electrotechnical Commission/Institute of Electrical and Electronics Engineers, Geneva, Switzerland, Aug. 2016.
[39] *Medical Electrical Equipment: Part 2–33: Particular Requirements for the Basic Safety and Essential Performance of Magnetic Resonance Equipment for Medical Diagnosis*, document IEC 60601-2-33, 2002.
[40] *IEEE Recommended Practice for Measurements and Computations of Radio Frequency Electromagnetic Fields With Respect to Human Exposure to Such Fields, 100 kHz-300 GHz*, document C95.3.1-2010.
[41] V. S. Chaudhary, D. Kumar, and S. Kumar, "Gold-immobilized photonic crystal fiber-based SPR biosensor for detection of malaria disease in human body," *IEEE Sensors J.*, vol. 21, no. 16, pp. 17800–17807, Aug. 2021.
[42] V. S. Chaudhary, D. Kumar, and S. Kumar, "SPR-assisted photonic crystal fiber-based dual-wavelength single polarizing filter with improved performance," *IEEE Trans. Plasma Sci.*, vol. 49, no. 12, pp. 3803–3810, Dec. 2021.
[43] G. P. Mishra, D. Kumar, V. S. Chaudhary, and S. Kumar, "Design and sensitivity improvement of microstructured-core photonic crystal fiber based sensor for methane and hydrogen fluoride detection," *IEEE Sensors J.*, vol. 22, no. 2, pp. 1265–1272, Jan. 2022.
[44] V. S. Chaudhary, D. Kumar, G. P. Mishra, S. Sharma, and S. Kumar, "Plasmonic biosensor with gold and titanium dioxide immobilized on photonic crystal fiber for blood composition detection," *IEEE Sensors J.*, vol. 22, no. 9, pp. 8474–8481, May 2022.
[45] U.S. Department of Health and Human Services. (2016). *Reporting of Computational Modeling Studies in Medical Device Submissions—Guidance for Industry and Food and Drug Administration Staff*. [Online]. Available: https://www.fda.gov
[46] H. H. Pennes, "Analysis of tissue and arterial blood temperatures in the resting human forearm," *J. Appl. Physiol.*, vol. 1, no. 2, pp. 93–122, 1948.
[47] A. L. H. M. W. van Lier, A. N. T. J. Kotte, B. W. Raaymakers, J. J. W. Lagendijk, and C. A. T. van den Berg, "Radiofrequency heating induced by 7 T head MRI: Thermal assessment using discrete vasculature or pennes' bioheat equation," *J. Magn. Reson. Imag.*, vol. 35, no. 4, pp. 795–803, Apr. 2012.
[48] L. A. Zaremba, "FDA guidelines for magnetic resonance equipment safety," Center Devices Radiol. Health, Food, Drug Admin., Rockville, MD, USA, Tech. Rep., 2010. [Online]. Available: http://www.aapm.org/meetings/02AM/pdf/8356-8054.pdf

YOUNGDAE CHO (Graduate Student Member, IEEE) was born in Busan, South Korea, in 1993. He received the B.Sc. and M.S. degrees in biomedical engineering from the University of Ulsan, Ulsan, South Korea, in 2016 and 2018, respectively. He is currently pursuing the Ph.D. degree in electronic engineering with Hanyang University, Seoul, South Korea. His current research interests include implantable antennas and devices, wireless power transfer, magnetic resonance imaging, RF coils, and radio-frequency heating and safety. He was a recipient of the Second Prize for the Best Student Paper Competition 2016 by the Korea Communications Agency (KCA) and the Korean Institute of Electromagnetic Engineering and Science (KIEES).

HYOUNGSUK YOO (Senior Member, IEEE) received the B.Sc. degree in electrical engineering from Kyungpook National University, Daegu, South Korea, in 2003, and the M.Sc. and Ph.D. degrees in electrical engineering from the University of Minnesota, Minneapolis, MN, USA, in 2006 and 2009, respectively. In 2009, he joined as a Postdoctoral Associate at the Center for Magnetic Resonance Research, University of Minnesota. In 2010, he joined as a Senior EM/MRI Scientist at the Cardiac Rhythm Disease Management, Medtronic, MN, USA. From 2011 to 2018, he was an Associate Professor at the Department of Biomedical Engineering, School of Electrical Engineering, University of Ulsan, Ulsan, South Korea. He has been the CEO of E2MR—a startup company, since 2017. Since 2018, he has been an Associate Professor with the Department of Biomedical Engineering, Hanyang University, Seoul, South Korea. His current research interests include electromagnetic theory, numerical methods in electromagnetics, metamaterials, antennas, implantable devices, and magnetic resonance imaging in high-magnetic field systems. He was awarded the Third Prize for the Best Student Paper at the 2010 IEEE Microwave Theory and Techniques Society International Microwave Symposium.